Increasing productivity of laser powder bed fusion manufactured Hastelloy X through modification of process parameters

Journal of Manufacturing Processes 78 (2022) 231–241

Contents lists available at ScienceDirect

Journal of Manufacturing Processes

journal homepage: www.elsevier.com/locate/manpro

Increasing productivity of laser powder bed fusion manufactured Hastelloy X through modification of process parameters

Claudia Schwerz *, Fiona Schulz, Elanghovan Natesan, Lars Nyborg

Chalmers University of Technology, Department of Industrial and Material Science, Sweden

ARTICLE INFO

Keywords:
Productivity
Build rate
Nickel-based superalloy
Microstructure
Processing
Mechanical properties

ABSTRACT

One of the factors limiting the use of additive manufacturing, particularly powder bed processes, is their low productivity. An approach to increasing laser powder bed fusion (LPBF) build rate without costly hardware modifications is to alter process parameters. This study evaluates the possibilities to increase build rates through this route without compromising material quality. Equations for productivity are derived based on process parameters and build geometry, and applied on the process window for Hastelloy X in LPBF. It is demonstrated that virtually flaw-free parts can be printed at build rates that differ up to tenfold. To investigate potential variations in the microstructure and performance, Hastelloy X specimens manufactured at varying build rates were characterized. Electron backscattered diffraction (EBSD) analysis revealed that the specimen built at the lowest rate shows strong texture with columnar grains, while the specimen built at the highest rate presents significantly more random orientation and evident melt pool contours with pockets of very fine grains at the bottom. Despite the major differences in microstructure, the tensile properties do not necessarily vary substantially. Thus, the results indicate that the build rate of LPBF Hastelloy X can be significantly varied based on process parameters, still yielding consistent mechanical properties.

1. Introduction

Additive manufacturing, particularly laser powder bed fusion (LPBF), has gained increasing attention over the last several years for manufacturing complex, functional components. However, the typically low build rates associated with this process represent a major barrier to its widespread use as an industrial manufacturing technology [1–3]. The low productivity makes the technology costlier, hence less competitive in many industrial sectors [4] and largely limited to high added value applications with low production volumes for which elevated costs are acceptable [5].

Several strategies have been investigated to address the issue of low productivity, ranging from hardware modifications to the tailoring of process parameters. Approaches based on hardware modifications include implementing multiple laser sources [4], whereby distinct areas can be simultaneously processed, decreasing the total exposure time per layer and the total build time. Despite the advancing maturity of this strategy, which allowed its implementation in commercial machines [6], some quality concerns have been reported with the use of multiple lasers in LPBF, namely the increased number and size of spatter particles [7] and the formation of internal flaws, particularly for overlap zones [8]. Aiming to process a larger volume of material instantly, the use of higher power laser sources [9,10] was proposed. Considering that the default energy distribution profile of laser beams in commercially available machines is Gaussian, high localized point intensity in the center of the beam facilitates the formation of keyhole porosity and spattering [11]. Additionally, the Gaussian profile is reported to induce lack of fusion due to the low intensities at the peripheries of the beam [12]. Therefore, modification of the laser beam geometry has been suggested to optimize the energy absorption while avoiding the formation of flaws [11,13,14]. Another strategy to instantly process larger volumes of material is to increase the laser beam diameter [15,16]. As increasing the laser beam diameter results in loss of precision [17], enlarging the laser spot size through defocusing has been proposed as an alternative [12,17].

Productivity gains based on major hardware modifications are costly, and many of the proposed approaches are still under development and have only been verified on pilot scales. Thus, a more readily available strategy to increase build rates is necessary, in which the productivity potential of any given machine is maximized. Several

* Corresponding author at: Rännvägen 2, SE-412 96, Gothenburg, Sweden.
E-mail address: claudia.schwerz@chalmers.se (C. Schwerz).

https://doi.org/10.1016/j.jmapro.2022.04.013
Received 7 December 2021; Received in revised form 6 April 2022; Accepted 9 April 2022
Available online 20 April 2022

approaches have been taken aiming for high build rates through modification of process parameters. Achievement of higher build rates has been reported by increasing the nominal layer thickness [1,18] and by increasing the laser scan speed [19,20]. Alternatively, process parameters capable of producing material with high relative density were identified while focusing on the increase of a particular process parameter, layer thickness [5,21], scan speed [2], and both laser scan speed and hatch spacing [22]. Finally, maximization of the build area utilization was proposed to increase LPBF build rates [23]. This summary demonstrates that a unified approach to increase LPBF build rates is needed. The absence of build rate parametrization based on key process parameters hinders the development of structured strategies for minimization of the total build time.

This study aims to establish an accessible alternative to productivity increase while producing virtually flaw-free materials. The material investigated is the nickel-base superalloy Hastelloy X, which is used, for example, in petrochemical applications due to its high resistance to stress-corrosion cracking, and in components in the combustion zone of gas turbine engines due to its combination of oxidation resistance and high-temperature strength [24]. Considering the stringent quality requirements of these application areas and the risk of flaw formation when altering process parameters [25], internal flaws in Hastelloy X are thoroughly mapped in the process parameter space [26]. Next, acceptance criteria are established, and a process window is defined. The experimental results are plugged into process parameter-based equations of the build rate, thereby mapping attainable build rates within the process window. Finally, the variability in microstructure and monotonic tensile properties of virtually flaw-free materials subjected to various build rates is assessed.

2. Build rate as a function of key build parameters

In LPBF, the build time is mainly governed by exposure of the bulk region; hence the equations in this section are developed based on infill parameters. The hatch spacing h, which determines the distance between neighboring laser tracks, and the laser scan speed v, which is the laser's travel velocity, determine how fast the laser exposes an area A. The time interval $\Delta\tau_{e,_i}$ needed for the laser exposure of a single slice (layer) i where the parts in manufacture have a total cross-sectional area A_i, using scan speed v_i and hatch spacing h_i in the infill region is:

$$\Delta\tau_{e,_i} = \frac{A_i}{v_i h_i} \tag{1}$$

The total build time $\Delta\tau_{tot}$ is the sum of the time intervals for exposure of each layer $i = 1, 2, \ldots, n$, $(\Delta\tau_{e,\,i})$, and the time intervals for the transition between layers $\Delta\tau_{tr,\,i}$. The latter includes lowering the build plate to a safe level to avoid collision between recoater and part, movement of the recoater to the dosage position, movement of the build platform to one layer thickness below the level of the previous layer, raising of the dispenser system, and recoating.

$$\Delta\tau_{tot} = \sum_{i=1}^{n}\left(\Delta\tau_{e,i} + \Delta\tau_{tr,i}\right) \tag{2}$$

Assuming constant transition time between layers and constant build parameters v and h throughout the build, the total build time is:

$$\Delta\tau_{tot} = \frac{\sum_{i=1}^{n} A_i}{vh} + n\Delta\tau_{tr} \tag{3}$$

The build volume V can be expressed as the sum of the volumes processed in each layer, that is $V = \sum_{i=1}^{n}(A_i t_i)$, where t_i is the thickness of layer i. The build height H is the sum of all layer thicknesses, $H = \sum_{i=1}^{n} t_i$. Assuming the layer thickness is kept constant along the build, then $V = t\sum_{i=1}^{n} A_i$ and $H = nt$. Thus, the total build time can be expressed as:

$$\Delta\tau_{tot} = \frac{V}{vht} + \frac{H\Delta\tau_{tr}}{t} \tag{4}$$

The build rate B is defined as the ratio between total built volume V and total build time $\Delta\tau_{tot}$ and can be expressed as:

$$B = \frac{V}{\Delta\tau_{tot}} = \frac{Rvht}{R + \Delta\tau_{tr} vh} \tag{5}$$

where R is the average build area utilization, also expressed as V/H and equivalent to the average laser-exposed area throughout the build. This factor accounts for the utilization of the powder bed area and, for a fixed build volume, can be altered with the orientation of the parts. Hence, a simplified equation for build rate based on key process parameters, the transition time interval between layers and the build area utilization is obtained.

The build rate is a linear function of layer thickness, and a rational function of each of the factors scan speed, hatch distance and build area utilization. Considering the domain of the variables, these functions are monotonically increasing, i.e., the build rate increases with each of the factors v, h and R. However, these functions have horizontal asymptotes, which means that, even theoretically, the build rate cannot be indefinitely increased with the increase of the factors v, h and R.

3. Materials and methods

Hastelloy X specimens were manufactured in an EOS M290 machine (Electro Optical Systems GmbH), equipped with an Yb fiber laser of maximum nominal power of 400 W and focused beam diameter of 100 μm. The processing was done in argon atmosphere with an oxygen concentration of less than 0.10%. The specimens destined for microstructural analysis, schematized in Fig. 1A, were produced using stripe scan strategy with a constant layer rotation angle of 67°, fixed hatch spacing of 100 μm and varying laser power, scan speed and layer thickness, as per Table 1. The feedstock powder used was gas atomized EOS NickelAlloy HX, with chemical composition compliant with UNS N06002 and AMS 5390. For further information on specimen preparation for metallography and quantification of internal flaws, the reader is referred to [26], where a detailed investigation of the processability of Hastelloy X in LPBF has been conducted.

Microstructural investigation was performed through light optical microscopy (LOM) using a Zeiss Axioscope 7 (Carl Zeiss Microscopy GmbH) and through scanning electron microscopy (SEM), utilizing a field emission gun scanning electron microscope (FEG-SEM) Leo Gemini 1550 (Carl Zeiss Microscopy GmbH). The cross-section analyzed in LOM is schematized with a red dashed line in Fig. 1A. The grain structure of the virtually flaw-free Hastelloy X material produced with varying manufacturing parameters was investigated using the FEG-SEM equipped with an electron backscattered diffraction (EBSD) detector (Nordlys II, Oxford Instruments plc). Measurements were taken at an accelerating voltage of 20 kV and 1.5 μm step size and processed using AZtecCrystal software (Oxford Instruments plc) by performing wild spikes removal and noise reduction to seven nearest neighbors. The orientation maps are presented in standard IPF (inverse pole figure) coloring, and high angle grain boundaries are indicated through black lines with a misorientation >10°. EBSD maps were taken in the center of the cylindrical test specimens with sufficient distance from any edges to ensure analysis of the bulk material only, as indicated in Fig. 1.

Tensile specimens were manufactured oriented along with the build direction with a subset of the processing conditions used in microstructural investigation. The specimen geometry is depicted in Fig. 1B. Removal from the build plate was performed with electrical discharge machining (EDM). An Instron 8501 servo-hydraulic machine (Instron, Norwood, MA, USA) was used to perform uniaxial tests to establish the monotonic behavior of Hastelloy X at room temperature. The tests were performed using the Instron 2630–102 axial clip-on static extensometer

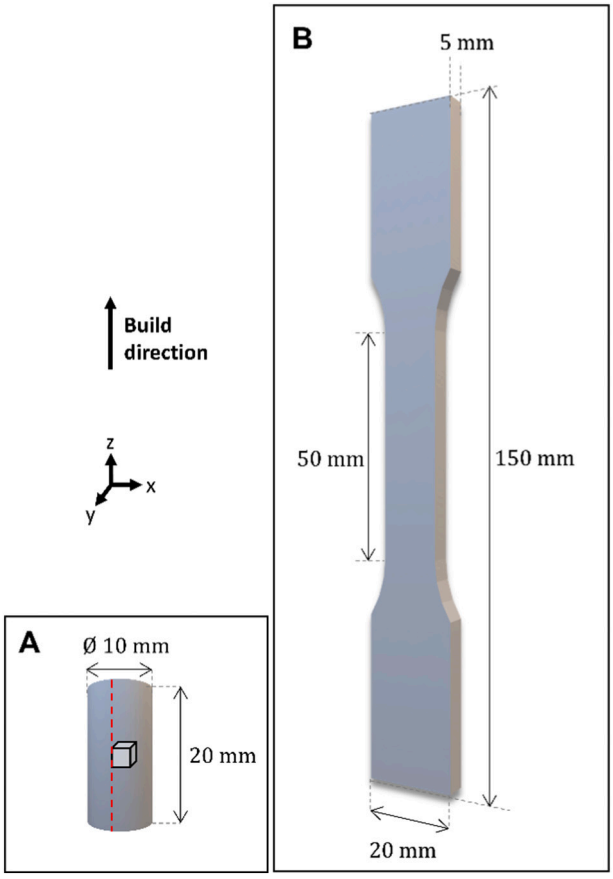

Fig. 1. Sketches of the specimens manufactured in this study and their orientations in relation to the build direction. (A) Geometry of the cylindrical specimens used for microstructural analysis. The red dashed line represents the cross-section analyzed in optical micrography. The faces of the cube represent the directions analyzed in EBSD. (B) Geometry of the tensile test specimens. (For interpretation of the references to colour in this figure legend, the reader is referred to the web version of this article.)

(Instron, Norwood, MA, USA), mounted on the gauge length for measuring the uniaxial strain. The tensile tests were performed at room temperature and at a strain rate of 0.01% s^{-1} in accordance with the ASTM E8/E8M guidelines [27].

4. Results

4.1. Determination of the process window

The internal flaws generated throughout the process parameter space in LPBF manufactured Hastelloy X have been mapped in previous work [26] using a process mapping approach [28,29]. Table 1 compiles the results, including the volume fraction of internal flaws. The allowance criteria for flaws depend on fitness for service [30] and cannot be determined universally. As the typical size and morphology of lack of fusion flaws turn them into important stress concentrators [31], process conditions that result in lack of fusion are not considered for the process window, regardless of their volume fraction. Regions of the process space where severe keyhole porosity is present are also excluded from the process window due to the irregular morphology and large keyhole pores accompanying the considerable volume fraction of flaws [26]. Process parameters that resulted in spherical pores of restricted size and volume fraction (approximately 0.1%) are considered to represent the process window due to the limited impact of these flaws in the mechanical properties and the possibility of eliminating them with hot isostatic pressing (HIP) [32]. The process conditions that fulfill these requirements are highlighted in Table 1. Systematic lack of fusion was observed in process conditions represented on the right-hand side of the highlighted cells, while systematic keyhole porosity was observed in the conditions represented on the left-hand side.

4.2. Quantification of build rates within the process window

Increasing productivity is only relevant in conditions for which the materials are fit for service, that is, within the process window. Therefore, the potential for build rate increase will be investigated within the process conditions defined in the previous section. From Eq. (5), the build rate depends on the laser scan speed, hatch spacing, layer thickness, build area utilization, and transition time between layers. However, from Table 1, it is observed that increased laser power widens the process window and shifts it to conditions that allow higher build rates. Thus, laser power is a variable that indirectly influences the build rate by influencing the location of the process window. The influence of laser power on build rates is illustrated in Fig. 2, in which the achievable build rate values or ranges, when applicable, are marked, according to the conditions highlighted in Table 1. The ratios between the highest and the lowest build rates attainable for each layer thickness are represented with dashed lines. Since a wider process window is identified for the layer thickness of 20 μm, greater relative improvements in the build rate ratios can be obtained. The maximum achievable build rate with a layer thickness of 20 μm is 8.6 cm^3/h, which is in the lower range attainable for a layer thickness of 40 μm and is considerably lower than the build rates attainable for the layer thickness of 80 μm.

The influence of layer thickness on the build rate within the process window is better visualized in Fig. 3A. The build rates achieved with a layer thickness of 40 μm are equal to or higher than those obtained with a layer thickness of 20 μm, and the build rates achieved with a layer thickness of 80 μm are the highest overall. In Fig. 3A, a build area utilization of 200 cm^2 is assumed, which corresponds to using one-third of the build area in the machine used in the present study on average throughout the build. Fig. 3B shows curves representing the build rates achieved with the parameters within the process window that allow for

Table 1
Volume fractions of flaws (%) across the process parameter space. Laser power, scan speed and layer thickness are varied systematically. "N/A" indicates manufacturing could not be completed due to extreme processing conditions. The highlighted cells correspond to process conditions considered desirable. Adapted from [26].

			Laser scan speed (mm/s)							
			200	400	600	800	1000	1200	1400	1600
Laser power: 100 W	Nominal layer thickness (μm)	20	0.39	0.01	0.31	1.41	5.48	7.97	11.6	14.2
		40	0.14	0.76	0.78	5.95	14.3	19.4	27.3	32.1
		80	5.61	11.7	16.5	26.8	35.1	45.4	N/A	N/A
Laser power: 200 W	Nominal layer thickness (μm)	20	4.47	2.55	0.03	0.01	<0.01	0.19	0.63	1.27
		40	5.12	2.77	0.02	0.01	0.09	0.44	1.67	4.51
		80	6.79	2.19	0.11	0.31	6.90	12.1	18.8	25.6
Laser power: 300 W	Nominal layer thickness (μm)	20	N/A	2.34	0.44	<0.01	<0.01	0.02	0.10	0.14
		40	3.31	3.50	0.30	<0.01	0.01	0.04	0.12	0.26
		80	4.50	3.19	0.35	0.01	0.03	0.06	0.39	2.53

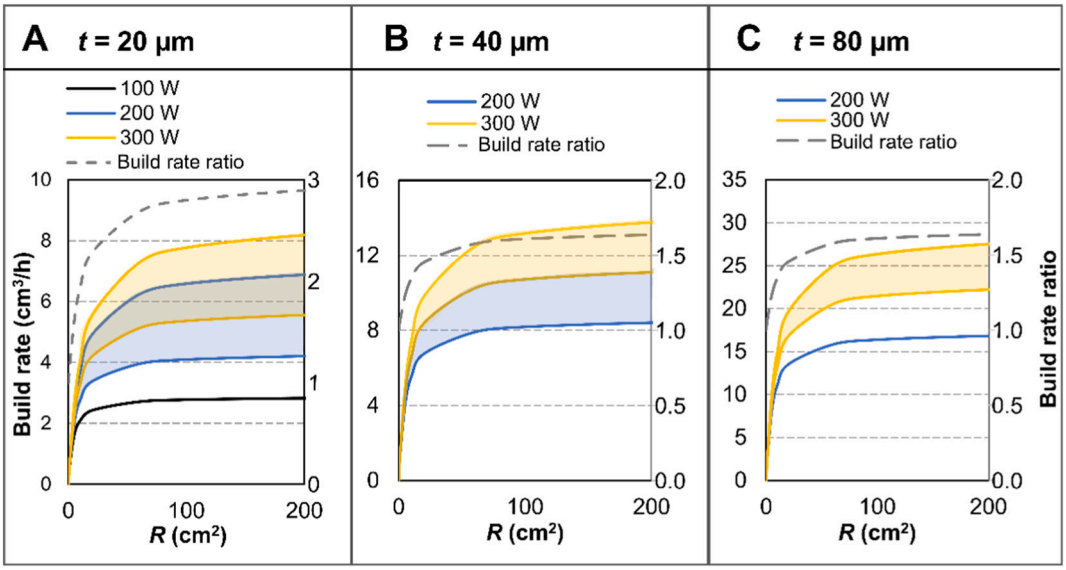

Fig. 2. Ranges of build rate in the process window for varying levels of laser power and layer thickness of 20 µm (A), 40 µm (B) and 80 µm (C). The dashed lines represent the ratios between the highest and lowest build rates attainable at each layer thickness.

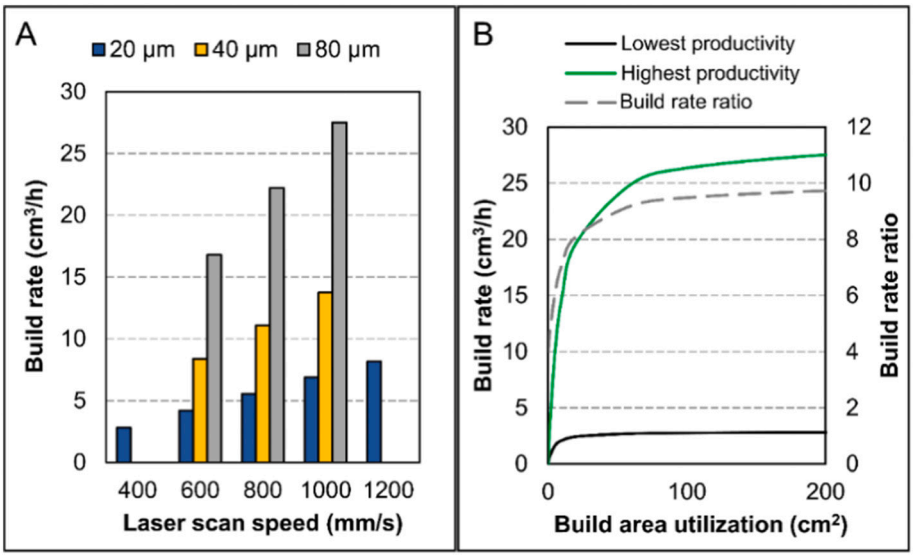

Fig. 3. Build rates (cm^3/h) for the processing conditions in the process window. The average utilization of the build area is assumed 200 cm^2 in (A). (B) Build rate as a function of the build area utilization for the parameters that enable highest and lowest productivities. The build rate ratio between these sets of parameters is also presented as a function of the build area utilization.

the highest and the lowest productivity as a function of the build area utilization. The ratio between the highest and lowest productivity is also represented. At low build area utilizations, the build rates obtained from these processing conditions differ by a factor of approximately 4. As the build area utilization increases, the ratios between build rates also increase, tending to a factor of 10 as R is increased indefinitely. Therefore, based on process parameters, the build rate can be increased by a minimum factor of 4 and up to approximately 10, depending on the part geometry and build area utilization, while producing virtually flaw-free material.

4.3. Variation in material structure across build rates

To determine whether an increase in productivity can be achieved without compromising quality, only virtually flaw-free specimens were considered for further analysis. As multiple process parameters were varied to increase productivity, some microstructural features are expected to vary within the defined process window. This subsection investigates the material structure of virtually flaw-free Hastelloy X manufactured in varying processing conditions.

The microstructure of LPBF manufactured Hastelloy X, as shown in Fig. 4, consists of the typical hierarchical microstructure of as-printed LPBF material [33]. The high temperature gradient promotes the formation of columnar grains that grow epitaxially in the build direction, visible in Fig. 4A together with melt pool boundaries. A cellular microstructure, which consists of high-density dislocation walls [34], is observed within the grains (Fig. 3C).

As macroscopic texture arises in additively manufactured material due to the epitaxial growth of grains from previous layers along the build direction [35], EBSD analysis was performed on selected specimens, as indicated in Table 2. Through this selection, the influence of each process parameter on the texture could be investigated within the process

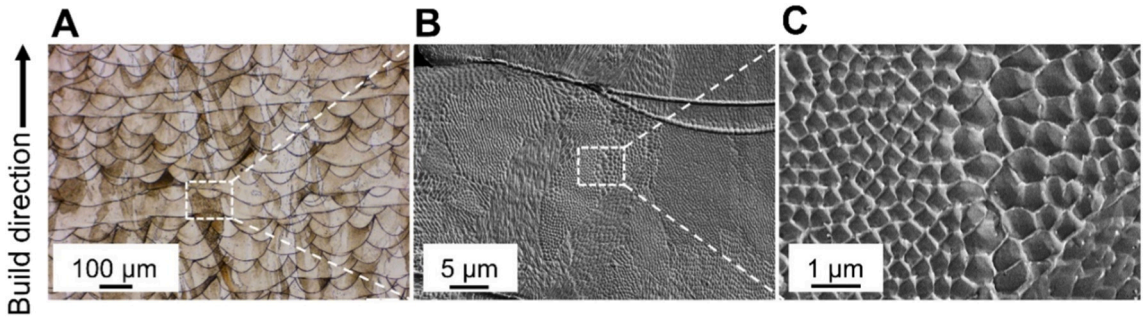

Fig. 4. Hierarchical microstructure of as-built Hastelloy X. (A) In the microstructure observed through light optical microscopy, columnar grains oriented along the build direction and melt pool boundaries are visible. (B) Through SEM imaging, the cellular microstructure is visible within grains. The well-defined lines are melt pool boundaries. (C) Detail on cell structure.

window. Specimens #1 and #2 represent the lowest and highest productivity output, respectively, from the previously down-selected parameters listed in Table 1. Specimens #3 and #4 were selected with respect to specimen #2 to isolate the influence of single parameter changes of laser scan speed and layer thickness, respectively. Specimen #5 relates to specimen #4 and shows the influence of decreasing laser power. Both the lowest and highest productivity specimens were investigated in detail in three directions. The comparative analysis of the iteratively changed parameter characteristics was performed on EBSD maps in the *xz* direction.

Fig. 5 shows EBSD orientation maps for all three orientations of specimens #1 and #2, which correspond to the lowest and highest theoretical productivity, respectively.

Specimen #1 shows strong ⟨101⟩ orientation, with columnar grains along the build direction. The cross-section perpendicular to the build direction (*xy* direction) shows that larger grains display the strong ⟨101⟩ orientation while smaller grains have more random orientation. The structure observed in specimen #2 is distinct and presents more random orientation and no columnar grains. Melt pool contours are visible in the orientation maps parallel to the build direction (*xz*- and *yz*- direction) for specimen #2 but not in the corresponding orientation maps for specimen #1. The grain size distributions are similar in both specimens and can be found in Fig. A.1 and Table A.1, Appendix A. The grain orientation maps for the material manufactured with the highest productivity show pockets of very fine grains at the bottom of the melt pool contours, while fine grains in the material manufactured with the lowest productivity are randomly distributed. As multiple process parameters were altered to increase productivity from lowest to highest, the influence of the individual parameters was investigated further.

Fig. 6 shows EBSD orientation maps of the specimens manufactured with varied process parameters and build rates. Compared to all other specimens, the material manufactured with the highest productivity (Fig. 5B) shows the most random grain orientation. Dropping the laser scan speed from 1000 mm/s to 800 mm/s removes the small grain clusters and introduces a stronger ⟨101⟩ orientation of the larger grains (Fig. 6C), while the melt pool contours remain visible. These contours disappear when decreasing the layer thickness from 80 µm to 20 µm while laser power and laser scan speed are kept constant with P = 300 W and v = 1000 mm/s (Fig. 6D). The decrease in layer thickness represents the most substantial difference in grain orientation and morphology, as the grains become columnar and display a strong ⟨101⟩ orientation. Reduction of the laser power from 300 W to 200 W re-introduces more randomly oriented grains (Fig. 6E) while still maintaining strong ⟨101⟩ texture. Summary statistics of the grain size distributions of all specimens in the *xz* plane can be found in Table A.2, Appendix A.

Fig. 7 depicts cross-sections of specimens #2 to #5, taken along the build direction and perpendicularly to the upmost scanning tracks. The images are taken at identical magnifications for better visualization of the melt pool dimensions and the extension of overlap between consecutive melt pools. Average and standard deviation values of melt pool depths are calculated based on a minimum of 30 measurements. Defining the average remelting ratio as the ratio between average melt pool depth and nominal layer thickness, the extent to which the material is remelted on each layer is estimated.

As the sole reduction of layer thickness does not significantly affect the melt pool dimensions [36], increased re-melted volume is obtained in specimen #4 in relation to specimen #2. As a result, directional grain growth along the build direction is promoted, leading to a strongly textured microstructure. Similarly, higher laser power increases the melt pool size and the energy input into the material, resulting in grain coarsening [37], which can be observed when comparing specimens #4 and #5. Reduction in the laser scan speed increases the amount of texture within the material, likely due to more significant heat retention that gives rise to more substantial epitaxial grain growth, similar to the effects of layer thickness and laser power. This trend is also reflected in the remelting ratio, which is increased for specimen #3 compared to specimen #2.

Table 2
Selection of manufacturing parameters for EBSD analysis.

Specimen	Laser power (W)	Laser scan speed (mm/s)	Layer thickness (µm)	Maximum theoretical productivity (cm^3/h)	Characteristic
#1	100	400	20	2.88	Lowest productivity
#2	300	1000	80	28.80	Highest productivity
#3	300	800	80	23.04	Δv compared to specimen #2
#4	300	1000	20	7.20	Δt compared to specimen #2
#5	200	1000	20	7.20	ΔP compared to specimen #4

4.4. Variation in tensile properties across build rates

To determine whether the investigated parameters influence the tensile properties of the material, tensile test specimens were manufactured using the same parameters (#1 to #5) as investigated in the previous section. The yield strength, ultimate tensile strength and elongation to fracture measured along the build direction for specimens manufactured with conditions #1 to #5 are summarized in Fig. 8. The average and standard deviation of a minimum of three tests are represented for each processing condition. Individual test results can be found in Table B.1, Appendix B. The average tensile properties of conditions

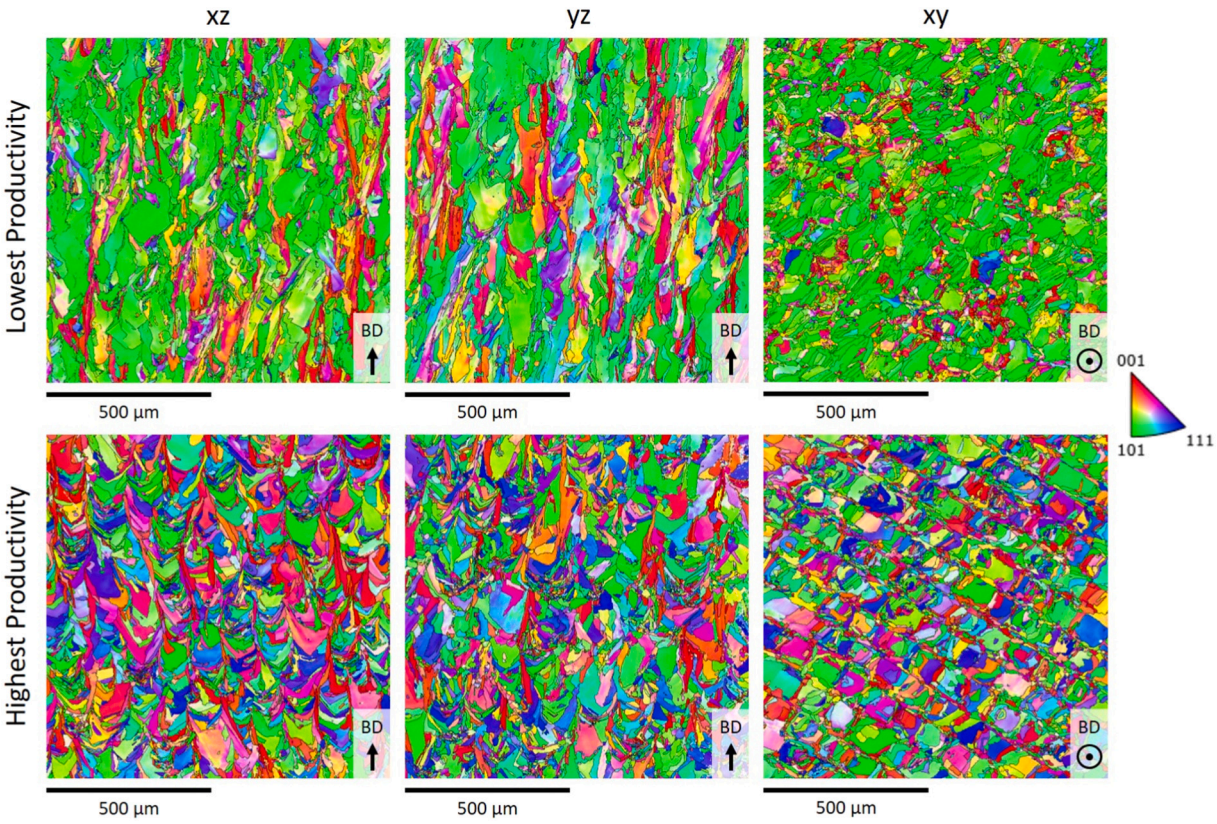

Fig. 5. EBSD orientation maps in IPF coloring for a specimen manufactured in condition #1 (lowest productivity with $P = 100$ W, v = 400 mm/s, $t = 0.02$ mm) and a specimen manufactured in condition #2 (highest productivity with $P = 300$ W, v = 1000 mm/s, $t = 0.08$ mm) for all sample orientations. Build direction is indicated for each orientation map with BD.

#1 and #2, which represent the extremes of the productivity range investigated, are comparable, with a 10% average yield strength as the most substantial difference. Condition #3, which differs from #2 by reduced laser scan speed, yields the lowest average yield and tensile strength. The average elongation values measured for conditions #3 and #5 are substantially lower than those obtained from the remaining conditions and than the values previously reported in the literature for similar conditions (as-built Hastelloy X along the build direction) [34,38].

5. Discussion

5.1. Quantifying productivity

The build rate of a single layer is the ratio between the volume processed in that layer $V_i = A_i t$ and the time interval for exposure of the layer, defined by Eq. (1):

$$B_i = \frac{V_i}{\Delta\tau_{e_{vj}}} = vht \tag{6}$$

The product obtained in Eq. (6) coincides with the most used metric for quantification of productivity. As this metric only quantifies the build rate of a single layer and does not account for the transition time between layers, it overestimates productivity and does not reflect the build rate of multilayered builds. The product of laser scan speed, hatch spacing and layer thickness is a reasonable approximation of the build rate of multilayered LPBF when the build area utilization is indefinitely increased or when the transition time between layers tends to zero. Hence, Eq. (6) represents a maximum theoretical value of build rate in multilayered builds.

The build rate of LPBF is highly dependent on the build layout, and high build rates rely on the efficient occupation of the machine's workspace volume [23]. This factor is often neglected, and the general aim tends to be to increase build rates through modification of process parameters alone. Some studies acknowledge the relevance of the build area utilization and include it in their optimization considerations, where the factor is termed bin packing [39] or nesting.

5.2. Influence of individual parameters on the build rate

Layer thickness is the process parameter present in Eq. (5) that yields the most expressive build rate increase when modified within the process window. However, large layer thicknesses result in a more important staircase effect, thereby compromising the surface finish, which is one of the main advantages of LPBF compared to other additive manufacturing processes [3]. To overcome this issue while enabling high build rates, several authors have proposed the application of a high-precision set of parameters on the contour of the parts and a high-productivity set of parameters in the bulk region in an approach referred to as “skin-core” [11] or “hull-bulk” [3] strategy. The increase in layer thickness has also been found to intensify spatter generation and, consequently, lack of fusion stemming from spatter redeposition on the powder bed [40]. While nominal layer thickness of 80 µm has been found to be relatively robust to flaws generated through this mechanism, significant lack of fusion has been demonstrated to occur upon further increase to 120 µm, thereby limiting further productivity increment [40].

As previously noted by Qiu et al. [41], higher laser power widens the process window. Larger melt pools allow for higher powder layer thicknesses and higher scan speeds for the laser to be employed. In the present study, the influence of laser power has been investigated at three levels (refer to Table 1), allowing for observation of this trend. In this

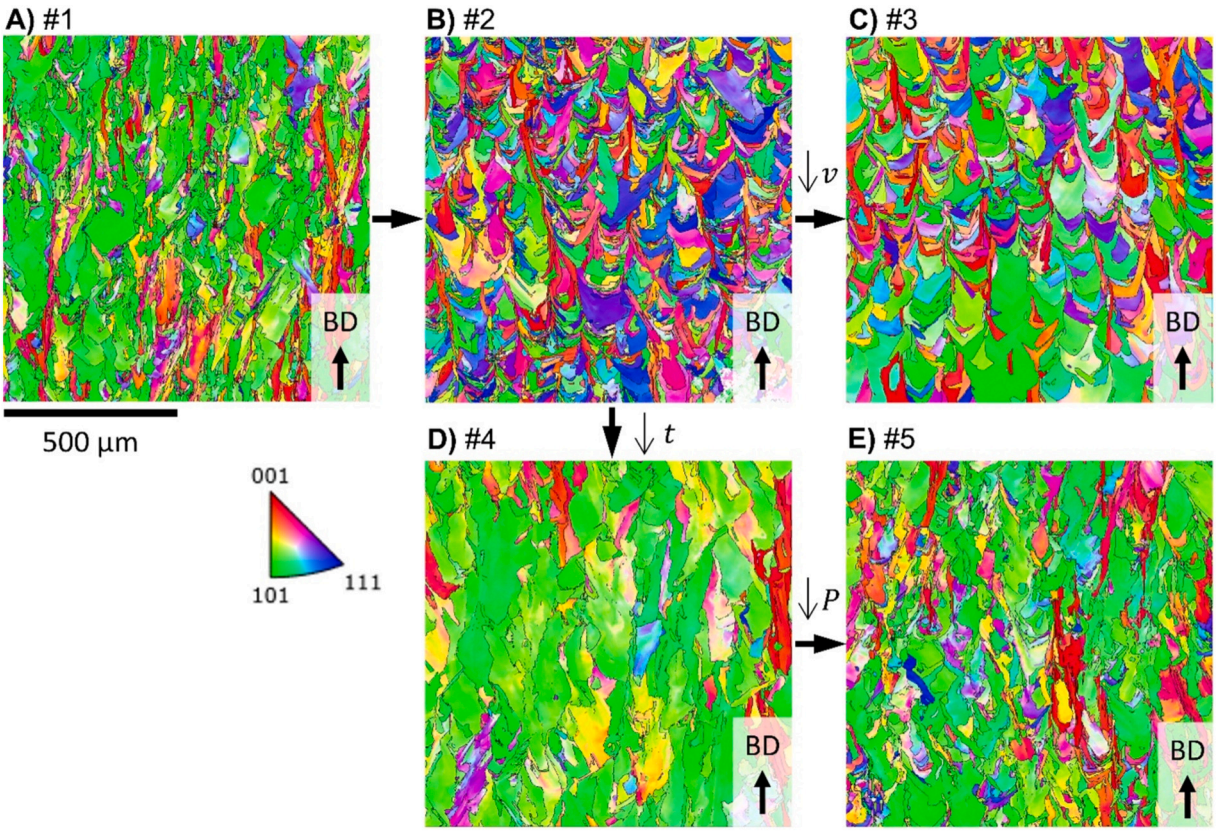

Fig. 6. EBSD orientation maps in IPF coloring for material manufactured with (A) the lowest productivity (condition #1 – $P = 100$ W, v = 400 mm/s, $t = 0.02$ mm), (B) the highest productivity (condition #2 - $P = 300$ W, v = 1000 mm/s, $t = 0.08$ mm), (C) decreased laser scan speed (condition #3 - $P = 300$ W, v = 800 mm/s, t = 0.08 mm), (D) decreased layer thickness (condition #4 - P = 300 W, v = 1000 mm/s, t = 0.02 mm), and (E) lowered laser power (condition #5 - $P = 200$ W, v = 1000 mm/s, t = 0.02 mm). The *xz* plane is depicted for all conditions.

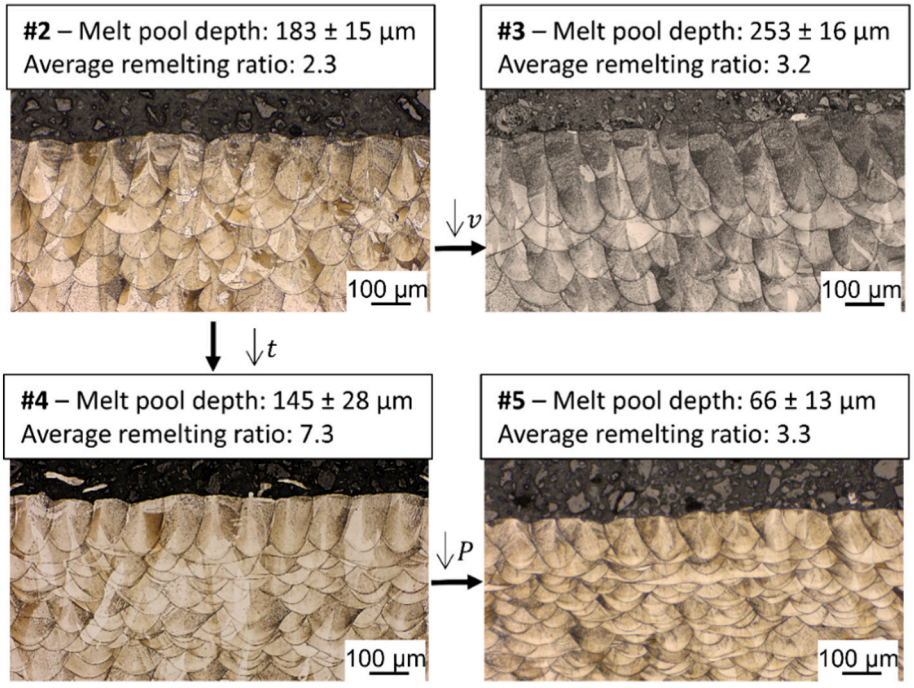

Fig. 7. Cross-sections of melt pools in the topmost layer of specimens #2 to #5 (A-D) parallel to the build direction and perpendicular to the upmost scanning tracks. The single process parameter variation among the specimens is schematized. The melt pool depths (average and standard deviation values) are presented for each specimen, as well as the average remelting ratio.

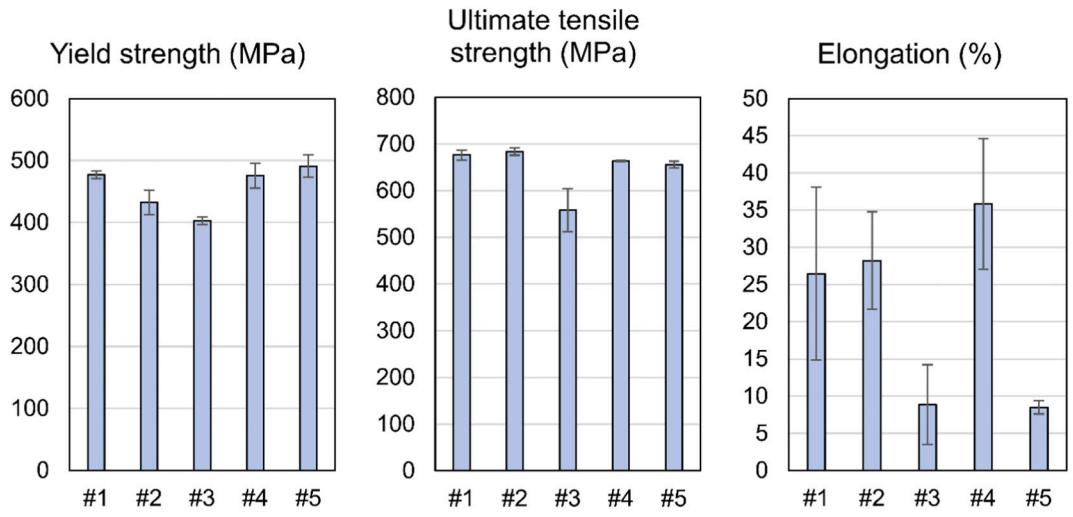

Fig. 8. Summary of tensile properties, conditions #1 to #5. Average and standard deviation of a minimum of three tests are represented for each condition.

study, the laser power has not been maximized in the experimental setup, as the nominal maximum laser power in the machine used is 400 W, which suggests that the process window can be further expanded, and the build rates further increased.

In this study, as defined in Section 4.1, the requirements for including a set of parameters in the process window are the absence of lack of fusion flaws and restricted pore content, approximately 0.1% maximum, and pores smaller than 100 μm. These criteria may be regarded as too conservative, as full densification following HIP has been reported in specimens with up to 5% porosity in the as-printed condition [32].

Considering the limitations previously presented (Fig. 2), up to a 3-fold build rate increase is possible by modifying the laser scan speed. However, together with the hatch spacing, the laser scan speed affects the time interval needed for the exposure of a layer, as expressed in Eq. (1), and consequently affects the interlayer time. Mohr et al. [42] define the interlayer time (ILT) as "the time span between subsequent energy input at a single volume element from layer to layer", which can be expressed as the transition time between layers added to the time needed to expose a layer:

$$ILT_i = \frac{A_i}{vh} + \Delta\tau_{tr} \tag{7}$$

Reduction of the interlayer time has been reported to result in heat accumulation and hardness drop over the build height [42], microstructure coarsening and reduction in yield and tensile strength [43], increase in residual stress levels and distortions [44].

The interlayer time depends on the transition time between layers, $\Delta\tau_{tr}$, measured as 9.3 s for the experimental conditions of the present study. This quantity can be minimized by maximizing the recoating speed, for example, but with limited gains in the global productivity and risks of uneven distribution of powder on the build area, which compromises the quality of the build. Thus, productivity increase through reduction of the interlayer time entails risks to part quality and homogeneity, which must be carefully assessed prior to implementation.

5.3. Variation in microstructure and properties with increasing build rates

The differences observed in the structure of materials manufactured with low and high productivity (Fig. 5) are due to the significant difference in scanning parameters (see Table 2), which affect the extension of the remelted area and the heat flow throughout the manufacturing process. The resulting solidification patterns can lead to significant differences in material texture [45]. Strong ⟨101⟩ orientation has previously been observed for additively manufactured FCC materials such as 316L [22] and Hastelloy X [38]. High volumetric energy density (VED) was linked to the presence of strong texture [46], which corresponds to the results in the present study, as specimen #1 was manufactured with $VED = 125\ J/mm^3$ and specimen #2 with $VED = 37.5 J/mm^3$.

Crystallographic orientation has a strong influence on the mechanical performance of LPBF nickel-based superalloys [46]. Knowledge of the influence of process parameters in material texture presents opportunities to increase manufacturing productivity and tailor material performance. Esmaeilizadeh et al. [47] demonstrated how the effect of adjusted scan speed and thus tailored grain structure could be used to optimize tensile properties of Hastelloy X material.

The conditions that output the two extreme productivities (#1 and #2, with maximum theoretical build rates of 2.88 and 28.8 cm^3/h, respectively) present significant differences in microstructure, but similar grain size distributions and tensile properties. The material displays the strongest texture and the heaviest right tail on the grain size distribution in the processing condition where a more important remelting effect is present (#4). The resulting yield and tensile strength are comparable to baseline condition #1 and the highest measured elongation to fracture.

Processing condition #3 resulted in the coarsest grains in average and an inferior combination of tensile properties. Comparing conditions #2 and #3, which are similar in terms of process parameters, the Hall-Petch effect explains the discrepancy in the measured yield strength, as #2 presents a smaller average grain size and exhibits higher yield strength. More importantly, condition #2 presents significantly higher ductility, which the grain size distribution can also explain. Grain refinement is one of the only routes towards strengthening and improving ductility simultaneously, thus breaking the inverse relationship often observed in other strengthening mechanisms. Based solely on the volume fraction of flaws, the tensile properties are not expected to vary between conditions #2 and #3. The measured fractions (0.03% and 0.01%, respectively) are considered residual for both cases, as the resulting relative densities are 99.93% and 99.99%, respectively. Considering that the flaws observed in this study are uniformly distributed on the cross-sections analyzed [26], such low levels of internal flaws do not substantially reduce the effective load-bearing cross-section and are not expected to affect the tensile properties.

It is clear from the present study that the observed differences in material structure for various processing parameter settings need to be investigated further despite the nominally flaw-free material. The rationalized equations and methodologies presented are proposed to provide a generic approach for deciding on and optimizing productivity increase strategies for LPBF.

6. Conclusions

In this study, the possibility of increasing the build rate while maintaining the quality of LPBF manufactured Hastelloy X was investigated. Firstly, the build rate was parametrized based on key process parameters and utilization of the build area. Next, by applying acceptance criteria to flaws identified in a detailed study of the processability of this alloy, a process window was defined, and it was possible to calculate the build rates in these processing conditions. Then, the microstructure and tensile properties were characterized in specimens produced with distinct build rates to identify variability and potential quality issues. The main findings of the present study are summarized below.

- The build rate is a linear function of layer thickness and a rational function of each of the factors laser scan speed, hatch spacing and build area utilization. All functions are monotonically increasing, but the rational functions have a horizontal asymptote that represents theoretical limits for build rate increase.
- Solely based on process parameters, the build rate can be increased by a minimum factor of 4 and up to 10, depending on the part geometry and utilization of the build area, while producing virtually flaw-free material.
- Laser power is a variable that indirectly influences the build rate by influencing the location of the process window, shifting it to conditions that allow higher productivity. Increasing laser power enlarges the melt pools, thus promoting more remelting, stronger texture and epitaxial grain growth.
- The main direct gain in productivity within the process window is obtained by increasing the layer thickness. As melt pool geometry is not significantly affected by the layer thickness employed, increasing this process parameter reduces the remelting zone, resulting in finer, more randomly oriented grains.
- The product *vht* is an overestimated measurement of build rate and does not reflect the influence of these process parameters in the build rate, which can be expressed as

$$B = \frac{Rvht}{R + \Delta\tau_{tr} vh}$$

- Stronger ⟨101⟩ orientation is consistently obtained when remelting larger volumes of material, independently of the process parameter varied. This is due to the competitive growth occurring preferentially in the easy-growth direction upon increased energy input provided by continued remelting.
- The results indicate that grain size distribution has the most significant influence on the average tensile properties along the build direction.

Declaration of competing interest

The authors declare that they have no known competing financial interests or personal relationships that could have appeared to influence the work reported in this paper.

Acknowledgments

This research was funded by European Union's Horizon 2020 research and innovation programme under grant agreement 820774, through project MANUELA—Additive Manufacturing using Metal Pilot Line. This work was conducted within the framework of the Centre for Additive Manufacturing—Metal (CAM2), supported by the Swedish Governmental Agency of Innovation Systems (Vinnova) under grant number 2016-05175. The authors thank Electro Optical Systems Finland Oy for providing the feedstock powder utilized in this research. Support from the Production Area of Advance at Chalmers is also acknowledged.

Appendix A

Table A.1
Summary statistics of the grain size distributions of specimen #1 (lowest productivity) and specimen #2 (highest productivity). The data are based on three different EBSD maps, each taken in the center of LPBF specimens for all three directions using a step size of 1.5 μm with a magnification of 100 times over an area of 1125 × 850 μm^2.

			Equivalent grain diameter [μm]			
Direction	Specimen	No. of grains	Maximum	Median	Mean	Standard deviation
xy	#1	10,892	111.2	10.7	14.1	10.4
	#2	8483	143.8	11.7	15.6	12.0
xz	#1	5405	174.6	12.0	17.1	15.3
	#2	5728	155.5	12.8	17.9	15.4
yz	#1	4784	168.3	12.6	17.9	16.3
	#2	6418	154.7	12.4	17.3	14.2

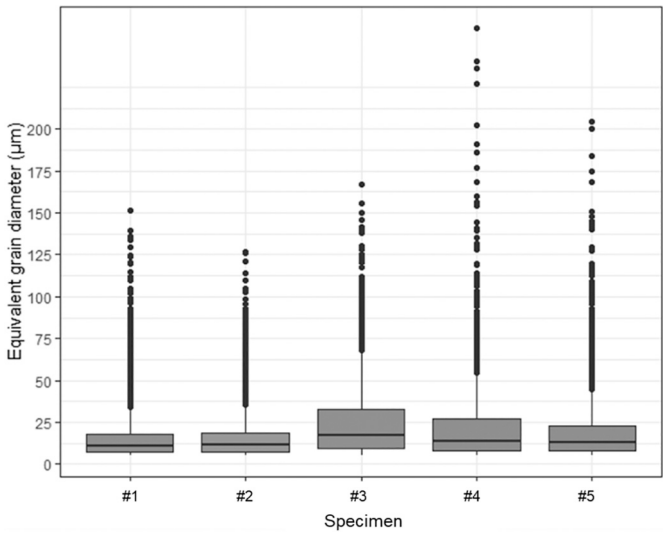

Fig. A.1. Grain size distributions measured in the build direction in specimens manufactured under conditions #1 to #5 in the *xz* plane.

Table A.2
Summary statistics of the grain size distributions of specimens #1 to #5. The data are based on three different EBSD maps, each taken in the center of the LPBF specimens in the *xz* plane, parallel to the build direction, using a step size of 1.5 µm with a magnification of 100 times over an area of 1125 × 850 µm^2.

		Equivalent grain diameter [µm]			
Specimen	No. of grains	Maximum	Median	Mean	Standard deviation
#1	5405	174.6	12.0	17.1	15.3
#2	5728	155.5	12.8	17.9	15.4
#3	2878	167.3	17.1	25.1	22.1
#4	1558	260.3	13.9	23.7	27.5
#5	4776	204.7	12.8	18.8	17.6

Appendix B

Table B.1
Individual tensile test results for processing conditions #1 to #5.

Condition	P (W)	v (mm/s)	t (µm)	Test ID	E (GPa)	YS (MPa)	UTS (MPa)	Elongation (%)
#1	100	400	20	1	193.8	471.88	682.37	31.9
#1	100	400	20	2	192.6	484.12	682.49	34.35
#1	100	400	20	3	184.5	475.96	664.09	13.11
#2	300	1000	80	1	187.4	422.98	683.13	33.91
#2	300	1000	80	2	178.3	412.31	682.88	33.62
#2	300	1000	80	3	182.2	437.87	671.31	20.04
#2	300	1000	80	4	236.3	425.58	691.46	31.09
#2	300	1000	80	5	166.6	463.89	688.89	22.31
#3	300	800	80	1	171.3	403.93	533.02	6.377
#3	300	800	80	2	180.6	408.37	529.38	5.181
#3	300	800	80	3	204.8	396.29	611.55	14.97
#4	300	1000	20	1	204.3	498.79	663.93	29.07
#4	300	1000	20	2	233.7	466.36	662.27	45.76
#4	300	1000	20	3	238.4	461.77	664.36	32.66
#5	200	1000	20	1	188.4	487.3	648.17	7.443
#5	200	1000	20	2	210.4	474.75	657.86	8.965
#5	200	1000	20	3	184.7	510.39	661.47	9.002

References

[1] Ma M, Wang Z, Gao M, Zeng X. Layer thickness dependence of performance in high-power selective laser melting of 1Cr18Ni9Ti stainless steel. J Mater Process Technol 2015;215:142–50. https://doi.org/10.1016/j.jmatprotec.2014.07.034.
[2] Sun Z, Tan X, Tor SB, Yeong WY. Selective laser melting of stainless steel 316L with low porosity and high build rates. Mater Des 2016. https://doi.org/10.1016/j.matdes.2016.05.035.
[3] de Formanoir C, Paggi U, Colebrants T, Thijs L, Li G, Vanmeensel K, Van Hooreweder B. Increasing the productivity of laser powder bed fusion: influence of the hull-bulk strategy on part quality, microstructure and mechanical performance of ti-6Al-4V. Addit Manuf 2020;33. https://doi.org/10.1016/j.addma.2020.101129.
[4] Attaran M. The rise of 3-D printing: the advantages of additive manufacturing over traditional manufacturing. Bus Horiz 2017;60:677–88. https://doi.org/10.1016/J.BUSHOR.2017.05.011.

[5] Leicht A, Fischer M, Klement U, Nyborg L, Hryha E. Increasing the productivity of laser powder bed fusion for stainless steel 316L through increased layer thickness. J Mater Eng Perform 2021;30:575–84. https://doi.org/10.1007/s11665-020-05334-3.

[6] Poprawe R, Hinke C, Meiners W, Schrage J, Bremen S, Merkt S. In: SLM production systems: recent developments in process development, machine concepts and component design. Cham: Springer; 2015. p. 49–65. https://doi.org/10.1007/978-3-319-12304-2_5.

[7] Taheri Andani M, Dehghani R, Karamooz-Ravari MR, Mirzaeifar R, Ni J. Spatter formation in selective laser melting process using multi-laser technology. Mater Des 2017;131:460–9. https://doi.org/10.1016/j.matdes.2017.06.040.

[8] Li S, Yang J, Wang Z. Multi-laser powder bed fusion of ti-6.5Al-2Zr-mo-V alloy powder: defect formation mechanism and microstructural evolution. Powder Technol 2021;384:100–11. https://doi.org/10.1016/j.powtec.2021.02.010.

[9] Buchbinder D, Schleifenbaum H, Heidrich S, Meiners W, Bültmann J. High power selective laser melting (HP SLM) of aluminum parts. Phys Procedia 2011;12:271–8. https://doi.org/10.1016/j.phpro.2011.03.035.

[10] Schleifenbaum H, Meiners W, Wissenbach K, Hinke C. Individualized production by means of high power selective laser melting. CIRP J Manuf Sci Technol 2010;2:161–9. https://doi.org/10.1016/j.cirpj.2010.03.005.

[11] Schleifenbaum H, Diatlov A, Hinke C, Bültmann J, Voswinckel H. Direct photonic production: towards high speed additive manufacturing of individualized goods. Prod Eng 2011;5:359–71. https://doi.org/10.1007/s11740-011-0331-0.

[12] Soylemez E. High deposition rate approach of selective laser melting through defocused single bead experiments and thermal finite element analysis for ti-6Al-4V. Addit Manuf 2020;31. https://doi.org/10.1016/j.addma.2019.100984.

[13] Gusarov AV, Grigoriev SN, Volosova MA, Melnik YA, Laskin A, Kotoban DV, Okunkova AA. On productivity of laser additive manufacturing. J Mater Process Technol 2018;261:213–32. https://doi.org/10.1016/j.jmatprotec.2018.05.033.

[14] Okunkova AA, Peretyagin PY, Podrabinnik PA, Zhirnov IV, Gusarov AV. Development of laser beam modulation assets for the process productivity improvement of selective laser melting. In: Procedia IUTAM. Elsevier B.V; 2017. p. 177–86. https://doi.org/10.1016/j.piutam.2017.06.019.

[15] Makoana N, Yadroitsava I, Möller H, Yadroitsev I. Characterization of 17–4PH single tracks produced at different parametric conditions towards increased productivity of LPBF Systems—The effect of laser power and spot size upscaling. Metals (Basel) 2018;8:475. https://doi.org/10.3390/met8070475.

[16] Shi W, Liu Y, Shi X, Hou Y, Wang P, Song G. Beam diameter dependence of performance in thick-layer and high-power selective laser melting of ti-6Al-4V. Materials (Basel) 2018;11. https://doi.org/10.3390/ma11071237.

[17] Metelkova J, Kinds Y, Kempen K, de Formanoir C, Witvrouw A, Van Hooreweder B. On the influence of laser defocusing in selective laser melting of 316L. Addit Manuf 2018;23:161–9. https://doi.org/10.1016/j.addma.2018.08.006.

[18] Shi X, Ma S, Liu C, Chen C, Wu Q, Chen X, Lu J. Performance of high layer thickness in selective laser melting of Ti6Al4V. Materials (Basel) 2016;9. https://doi.org/10.3390/ma9120975.

[19] Pauzon C, Leicht A, Klement U, Forêt P, Hryha E. Effect of the process gas and scan speed on the properties and productivity of thin 316L structures produced by laser-powder bed fusion. Metall Mater Trans A Phys Metall Mater Sci 2020;51:5339–50. https://doi.org/10.1007/s11661-020-05923-w.

[20] Pauzon C, Forêt P, Hryha E, Arunprasad T, Nyborg L. Argon-helium mixtures as laser-powder bed fusion atmospheres: towards increased build rate of ti-6Al-4V. J Mater Process Technol 2020;279:116555. https://doi.org/10.1016/j.jmatprotec.2019.116555.

[21] Wang S, Liu Y, Shi W, Qi B, Yang J, Zhang F, Han D, Ma Y. Research on high layer thickness fabricated of 316L by selective laser melting. Materials (Basel) 2017;10. https://doi.org/10.3390/ma10091055.

[22] Leicht A, Rashidi M, Klement U, Hryha E. Effect of process parameters on the microstructure, tensile strength and productivity of 316L parts produced by laser powder bed fusion. Mater Charact 2019. https://doi.org/10.1016/j.matchar.2019.110016.

[23] Kostevsek U, Brajlih T, Balic J, Kadivnik Ž, Drstvensek I. Development of productivity estimation model for mass-customized production by selective laser melting. Rapid Prototyp J 2018;24:670–6. https://doi.org/10.1108/RPJ-06-2017-0120.

[24] Haynes International, (n.d.). https://www.haynesintl.com/alloys/alloy-portfolio_/High-temperature-Alloys/HASTELLOY-X-alloy.

[25] Kose H, Jin M, Peng T. Quality and productivity trade-off in powder-bed additive manufacturing. Prog Addit Manuf 2020;5:199–210. https://doi.org/10.1007/s40964-020-00122-w.

[26] Schwerz C, Nyborg L. Linking in situ melt pool monitoring to melt pool size distributions and internal flaws in laser powder bed fusion. Met. 2021;11:1856. https://doi.org/10.3390/MET11111856. 2021, Vol. 11, Page 1856.

[27] A. International. ASTM E8/E8M - 13 standard test methods for tension testing of metallic materials. 2013.

[28] Beuth J, Klingbeil N. The role of process variables in laser-based direct metal solid freeform fabrication. JOM 2001;53:36–9. https://doi.org/10.1007/s11837-001-0067-y.

[29] Beuth J, Fox J, Gockel J, Montgomery C, Yang R, Qiao H, Soylemez E, Reeseewatt P, Anvari A, Narra S, Klingbeil N. Process mapping for qualification across multiple direct metal additive manufacturing processes. In: 24th Int. SFF Symp. - An Addit. Manuf. Conf. SFF 2013. University of Texas at Austin (freeform); 2013. p. 655–65.

[30] ASM Handbook. Failure Analysis and Prevention, 11; 2002. http://books.google.com.hk/books?id=eC-Zt1J4oCgC.

[31] Snow Z, Nassar AR, Reutzel EW. Invited review article: review of the formation and impact of flaws in powder bed fusion additive manufacturing. Addit Manuf 2020;36. https://doi.org/10.1016/j.addma.2020.101457.

[32] Herzog D, Bartsch K, Bossen B. Productivity optimization of laser powder bed fusion by hot isostatic pressing. Addit Manuf 2020;36. https://doi.org/10.1016/j.addma.2020.101494.

[33] Wang YM, Voisin T, McKeown JT, Ye J, Calta NP, Li Z, Zeng Z, Zhang Y, Chen W, Roehling TT, Ott RT, Santala MK, Depond PJ, Matthews MJ, Hamza AV, Zhu T. Additively manufactured hierarchical stainless steels with high strength and ductility. Nat. Mater 2017;171(17):63–71. https://doi.org/10.1038/nmat5021. 2017.

[34] Montero-Sistiaga ML, Liu Z, Bautmans L, Nardone S, Ji G, Kruth JP, Van Humbeeck J, Vanmeensel K. Effect of temperature on the microstructure and tensile properties of micro-crack free hastelloy X produced by selective laser melting. Addit Manuf 2020;31:100995. https://doi.org/10.1016/J.ADDMA.2019.100995.

[35] DebRoy T, Wei HL, Zuback JS, Mukherjee T, Elmer JW, Milewski JO, Beese AM, Wilson-Heid A, De A, Zhang W. Additive manufacturing of metallic components – process, structure and properties. Prog Mater Sci 2018;92:112–224. https://doi.org/10.1016/j.pmatsci.2017.10.001.

[36] Keshavarzkermani A, Marzbanrad E, Esmaeilizadeh R, Mahmoodkhani Y, Ali U, Enrique PD, Zhou NY, Bonakdar A, Toyserkani E. An investigation into the effect of process parameters on melt pool geometry, cell spacing, and grain refinement during laser powder bed fusion. Opt Laser Technol 2019;116:83–91. https://doi.org/10.1016/j.optlastec.2019.03.012.

[37] Zhang X, Yocom CJ, Mao B, Liao Y. Microstructure evolution during selective laser melting of metallic materials: a review. J Laser Appl 2019;31:031201. https://doi.org/10.2351/1.5085206.

[38] Keshavarzkermani A, Esmaeilizadeh R, Ali U, Enrique PD, Mahmoodkhani Y, Zhou NY, Bonakdar A, Toyserkani E. Controlling mechanical properties of additively manufactured hastelloy X by altering solidification pattern during laser powder-bed fusion. Mater Sci Eng A 2019;762:138081. https://doi.org/10.1016/j.msea.2019.138081.

[39] Griffiths V, Scanlan JP, Eres MH, Martinez-Sykora A, Chinchapatnam P. Cost-driven build orientation and bin packing of parts in selective laser melting (SLM). Eur J Oper Res 2019;273:334–52. https://doi.org/10.1016/j.ejor.2018.07.053.

[40] Schwerz C, Raza A, Lei X, Nyborg L, Hryha E, Wirdelius H. In-situ detection of redeposited spatter and its influence on the formation of internal flaws in laser powder bed fusion. Addit Manuf 2021:102370. https://doi.org/10.1016/J.ADDMA.2021.102370.

[41] Qiu C, Panwisawas C, Ward M, Basoalto HC, Brooks JW, Attallah MM. On the role of melt flow into the surface structure and porosity development during selective laser melting. Acta Mater 2015;96:72–9. https://doi.org/10.1016/j.actamat.2015.06.004.

[42] Mohr G, Altenburg SJ, Hilgenberg K. Effects of inter layer time and build height on resulting properties of 316L stainless steel processed by laser powder bed fusion. Addit Manuf 2020;32:101080. https://doi.org/10.1016/j.addma.2020.101080.

[43] Xu W, Lui EW, Pateras A, Qian M, Brandt M. In situ tailoring microstructure in additively manufactured ti-6Al-4V for superior mechanical performance. Acta Mater 2017;125:390–400. https://doi.org/10.1016/j.actamat.2016.12.027.

[44] Denlinger ER, Heigel JC, Michaleris P, Palmer TA. Effect of inter-layer dwell time on distortion and residual stress in additive manufacturing of titanium and nickel alloys. J Mater Process Technol 2015;215:123–31. https://doi.org/10.1016/j.jmatprotec.2014.07.030.

[45] Wei HL, Mazumder J, DebRoy T. Evolution of solidification texture during additive manufacturing. Sci. Reports 2015;5:1–7. https://doi.org/10.1038/srep16446. 2015 51.

[46] Sanchez-Mata O, Wang X, Muñiz-Lerma JA, Atabay SE, Attarian Shandiz M, Brochu M. Dependence of mechanical properties on crystallographic orientation in nickel-based superalloy hastelloy X fabricated by laser powder bed fusion. J Alloys Compd 2021;865:158868. https://doi.org/10.1016/J.JALLCOM.2021.158868.

[47] Esmaeilizadeh R, Keshavarzkermani A, Ali U, Mahmoodkhani Y, Behravesh B, Jahed H, Bonakdar A, Toyserkani E. Customizing mechanical properties of additively manufactured hastelloy X parts by adjusting laser scanning speed. J Alloys Compd 2020;812. https://doi.org/10.1016/j.jallcom.2019.152097.